Advances in Intelligent Systems and Computing 283

Ewa Pietka
Jacek Kawa
Wojciech Wieclawek *Editors*

Information Technologies in Biomedicine, Volume 3

Springer

Advances in Intelligent Systems and Computing

Volume 283

Series editor

Janusz Kacprzyk, Polish Academy of Sciences, Warsaw, Poland
e-mail: kacprzyk@ibspan.waw.pl

For further volumes:
http://www.springer.com/series/11156

About this Series

The series "Advances in Intelligent Systems and Computing" contains publications on theory, applications, and design methods of Intelligent Systems and Intelligent Computing. Virtually all disciplines such as engineering, natural sciences, computer and information science, ICT, economics, business, e-commerce, environment, healthcare, life science are covered. The list of topics spans all the areas of modern intelligent systems and computing.

The publications within "Advances in Intelligent Systems and Computing" are primarily textbooks and proceedings of important conferences, symposia and congresses. They cover significant recent developments in the field, both of a foundational and applicable character. An important characteristic feature of the series is the short publication time and world-wide distribution. This permits a rapid and broad dissemination of research results.

Advisory Board

Ewa Pietka · Jacek Kawa
Wojciech Wieclawek
Editors

Information Technologies in Biomedicine, Volume 3

Springer

Editors
Ewa Pietka
Silesian University of Technology
Faculty of Biomedical Engineering
Gliwice
Poland

Wojciech Wieclawek
Silesian University of Technology
Faculty of Biomedical Engineering
Gliwice
Poland

Jacek Kawa
Silesian University of Technology
Faculty of Biomedical Engineering
Gliwice
Poland

ISSN 2194-5357 ISSN 2194-5365 (electronic)
ISBN 978-3-319-06592-2 ISBN 978-3-319-06593-9 (eBook)
DOI 10.1007/978-3-319-06593-9
Springer Cham Heidelberg New York Dordrecht London

Library of Congress Control Number: 2008926730

Preface

In clinical application we deal with problems that have to be solved in a fast and objective way. However, human observation is influenced by internal (coming form the observer) as well as external (often independent from the observer) impacts. The objectivity of classification is restricted by the receptivity of human senses which are influenced by the experiences or level of training, psychological conditions (tiredness, haste, etc.), as well as external conditions (lighting, destructive noise, etc.) A failure in perception questions the entire recognition process. The recognition process itself, influenced also by the above mentioned conditions, may cause a slowdown and/or lead to a false diagnosis.

New computerized approaches to various problems have become critically important in healthcare. Computer assisted diagnosis has been extended towards a support of the clinical treatment. Mathematical information analysis, computer applications together with medical equipment and instruments have become standard tools underpinning the current rapid progress with developing Computational Intelligence. We are witnessing a radical change as technologies have been integrated into systems that address the core of medicine, including patient care in ambulatory and in-patient setting, disease prevention, health promotion, rehabilitation and home care. A computerized support in the analysis of patient information and implementation of a computer aided diagnosis and treatment systems, increases the objectivity of the analysis and speeds up the response to pathological changes.

This book aims to present a variety of state-of-the-art information technology and its applications to the networked environment to allow robust computerized approaches to be introduced throughout the healthcare enterprise. Image and signal analysis are the traditional parts that deal with the problem of data processing, recognition and classification. Bioinformatics has become a dynamically developed field of computer assisted biological data analysis. Patients' safety and shortening of the rehabilitation time requires a more rapid development of minimally invasive surgery supported by image navigation techniques. Home care, remote rehabilitation assistance, safety of the elderly require new areas to be explored in telemedicine and telegeriatrics.

This book set is a continuation of a book series. This set contains two volumes. *Information Technologies in Biomedicine, Volume 3* discusses Image analysis techniques and their applications in healthcare, as well as some Bioinformatics issues. *Information Technologies in Biomedicine, Volume 4* consists of six parts including Computer Aided Surgery, Telemedicine, Telegeriatrics,

We would like to express our gratitude to the authors who contributed their original research papers as well as the reviewers for their valuable comments.

Ewa Pietka

Contents

Part I: Image Analysis and Applications

Applications of Ray-Casting in Medical Imaging 3
Maciej Borzęcki, Adam Skurski, Marek Kamiński, Andrzej Napieralski, Jarosław Kasprzak, Piotr Lipiec

A New Aortic Aneurysm CT Series Registration Algorithm 15
Joanna Czajkowska, Christian Feinen, Marcin Grzegorzek, Matthias Raspe, Ralph Wickenhöfer

Angular Resolution Study of Vectors Representing Subtle Spiculated Structures in Mammograms 27
Magdalena Jasionowska, Artur Przelaskowski

Line Segment Based Approach to Pattern Detection in Mammographic Images 37
Jagoda Lazarek, Piotr S. Szczepaniak

Breast Phantom Imaging Results from an Ultrasound Computer Tomography Research System 49
Krzysztof J. Opieliński, Piotr Pruchnicki, Tadeusz Gudra, Przemysław Podgórski, Tomasz Kraśnicki, Jacek Kurcz, Marek Sąsiadek

Adaptive Preprocessing of X-ray Hand Images 61
Marzena Bielecka, Adam Piórkowski

Cruciate Ligaments of the Knee Joint in the Computer Analysis 71
Piotr Zarychta

Trabecular Bone Microstructure Investigation 81
Paulina Popik, Marcin Binkowski, Łukasz Cyganik, Filip Bolechała, Roman Nowak, Antoni John, Zygmunt Wróbel

The Three Dimensional Visualization Growth of Bone Tissue in Microstructure of Surface Analysis Using Drishti Open-Source Software 91
Mateusz Stolarz, Krzysztof Ficek, Marcin Binkowski, Anna Wójcicka, Zygmunt Wróbel

Fractal Texture Analysis in the Irregular Region of Interest of the Healing Process Using Guided Bone Regeneration 103
Marta Borowska, Edward Oczeretko, Janusz Szarmach

A New Method of Automatic Craniometric Landmarks Definition and Soft Tissue Thickness Measurement Based on MRI Data 115
Iryna Gorbenko, Krzysztof Mikołajczyk, Iaroslav Iarovyi, Tomasz Kubik, Krzysztof Kałużyński

The Assessment of Brain Volume in the Postoperative Craniosynostosis 127
Anna Fabijańska, Jarosław Gocławski, Wanda Mikołajczyk-Wieczorek

Multi-Image Texture Analysis in Classification of Prostatic Tissues from MRI. Preliminary Results 139
Dorota Duda, Marek Kretowski, Romain Mathieu, Renaud de Crevoisier, Johanne Bezy-Wendling

Adaptive Sparse Recovery of Medical Images with Variational Approach – Preliminary Study for CT Stroke 151
Artur Przelaskowski

Application of the Digital Curvelet Transform for the Purpose of Image Denoising in MRI 165
Joanna Świebocka-Więk, Henryk Figiel

Universal Segmentation Framework for Medical Imaging Using Rough Sets Theory and Fuzzy Logic Clustering 175
Marcin Majak

Ultrafast Iterative Model-Based Statistical 3D Reconstruction Algorithm for X-ray Computed Tomography 187
Robert Cierniak, Michal Knas

Comparison Study of Two Programs Dedicated to X-ray Microtomography Data Analysis 197
Joanna Śróbka, Marcin Binkowski, Martyna Czaja, Iwona Szarejko, Zygmunt Wróbel

Object Detail Correspondence Problem in Stereovision 209
Pawel Popielski, Zygmunt Wróbel, Robert Koprowski

An Algorithm for the Pore Size Determination Using Digital Image Analysis 223
Małgorzata Charytanowicz

Automatic Car Make Recognition in Low-Quality Images 235
Paweł Badura, Maria Skotnicka

Retina Analysis in Optical Coherence Tomography Images 247
Wojciech Wieclawek, Ewa Pietka

Part II: Bioinformatics

Numerical Simulation of the Vascular Solid Tumour Growth Model and Therapy – Parallel Implementation 261
Krzysztof Psiuk-Maksymowicz, Damian Borys, Sebastian Student, Andrzej Świerniak

Searching for Malignancy in Automated Urological Cytology 271
Boguslaw D. Pietka, Annamonika Dulewicz

microRNA 3'-end Modification Detection Algorithm and Its Usage Example for Tissue Classification 285
Marta Danch, Damian Borys, Tomasz Stokowy, Knut Krohn, Krzysztof Fujarewicz

A Machine Learning Approach to Identify Prostate Cancer Areas in Complex Histological Images 295
Sadri Salman, Zhaoxuan Ma, Sambit Mohanty, Sanica Bhele, Yung-Tien Chu, Beatrice Knudsen, Arkadiusz Gertych

Spectral Classification of Dual Nuclear p16/Ki67 Positivity in Pap Smears 307
Sukhveer Sandhu Singh, Arkadiusz Gertych

Simulation Analysis of the ATR Module as a Detector of UV-Induced DNA Damage 317
Monika Kurpas, Katarzyna Jonak, Krzysztof Puszyński

Protein Hotspot Prediction Using S-Transform 327
Jan Kasparek, Denisa Maderankova, Ewaryst Tkacz

Extended Spatial Evolutionary Games and Induced Bystander Effect 337
Michał Krześlak, Andrzej Świerniak

Prediction of the Behavior of Mammalian Cells after Exposure to Ionizing Radiation Based on the New Mathematical Model of ATM-Mdm2-p53 Regulatory Pathway 349
Katarzyna Jonak, Monika Kurpas, Krzysztof Puszyński

Euler's and Taylor's Expansion Method Applied on Non-linear Pharmacokinetics Model 363
Daniela Gombárska, Mariana Beňová

Prokaryotic DNA Signal Downsampling for Fast Whole Genome Comparison 373
Karel Sedlar, Helena Skutkova, Martin Vitek, Ivo Provaznik

Using Analysis Algorithms and Image Processing for Quantitative Description of Colon Cancer Cells 385
Anna Wójcicka, Przemysław Jędrusik, Mateusz Stolarz, Robert Kubina, Zygmunt Wróbel

Relationship of Bacteria Using Comparison of Whole Genome Sequences in Frequency Domain 397
Vladimira Kubicova, Ivo Provaznik

Three-Step Framework of Feature Selection for Data of DNA Microarray Experiments 409
Pawel Trajdos, Adam Kamizelich, Marek Kurzynski

Author Index 421

Part I

Image Analysis and Applications

Applications of Ray-Casting in Medical Imaging

Maciej Borzęcki[1], Adam Skurski[1], Marek Kamiński[1], Andrzej Napieralski[1], Jarosław Kasprzak[2], and Piotr Lipiec[2]

[1] Department of Microelectronics and Computer Science, Lodz University of Technology, Łódź, Poland
mborzecki@dmcs.pl
[2] Department of Cardiology, Medical University of Lodz, Łódź, Poland

Abstract. The authors present applications of ray casting as segmentation and analysis method for processing of medical imaging data. The first application features ray casting based image segmentation for extraction of a region enclosing heart structures from a series of CT scans. Proposed method yields significant gains in reduction of the data set size, that are of importance in applications such as Transesophageal USG simulations on mobile devices or web platforms.

Another application, utilizes ray casting determining location of characteristic points of *left ventricle* (LV). The points are used as reference during automatic fusion of ECHO Automated Function Imaging output with a 3D model of LV.

Keywords: ray casting, image segmentation, computed tomography.

1 Introduction

Ray casting is a method that has seen wide use in a plethora of applications in different fields. Object picking within a 3D scene or collision detection are examples of traditional uses of ray casting [1, 2]. The method has also been successfully applied in the field of image processing for segmentation and extraction purpose. Example applications as described in [3, 4], indicate a level of success when method is applied for segmentation of medical imaging.

The core idea behind use of ray casting in image segmentation or feature location is largely unchanged from the typical approach. Virtual rays are emitted in a number of directions from a single origin point. For each iteration, a boundary condition is evaluated, indicating whether for the current location of the tip of the ray, the propagation can continue. In case of image segmentation, the boundary condition is typically a function testing if given point is within the desired data set. The concept is briefly visualized in Fig. 1.

Once the points where the ray propagation has ceased are established further steps are taken in order to create a mask or an outline of the identified structure. Typically employed methods are neighbor contour tracing [5] or construction of polygon by connecting the end points.

E. Pietka, J. Kawa, and W. Wieclawek (eds.), *Information Technologies in Biomedicine, Volume 3*, Advances in Intelligent Systems and Computing 283,
DOI: 10.1007/978-3-319-06593-9_1,

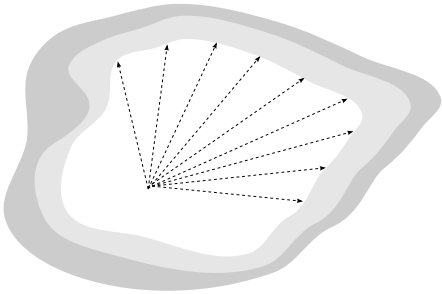

Fig. 1. Ray casting for image segmentation

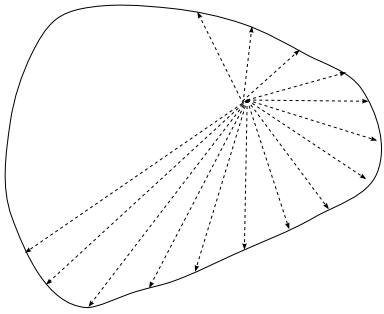

Fig. 2. Ray casting within a convex shape

Ray casting as a method is a subject to a number of problems that need to tackled with. The first problem is the shape of the object under consideration. As shown in Fig. 2, convex shapes usually yield good results.

For concave shapes, such as one shown in Fig. 3, location of ray origin point poses a problem. Misplaced origin will amplify the shadowing, the effect of which needs to be taken into consideration.

If the structure being extracted is relatively large, one needs to consider how many rays need to cast in order to obtain a reasonably good set of points for analysis. The problem is caused by the fact that only a certain number of rays is practical for most applications. In case of image segmentation, too few points may negatively affect the process of establishing object contour.

In the following sections the authors discuss ray casting as a method for processing medical imaging data, where Section 2 describes application in image segmentation, and Section 3 covers automated location of features in a 3D model.

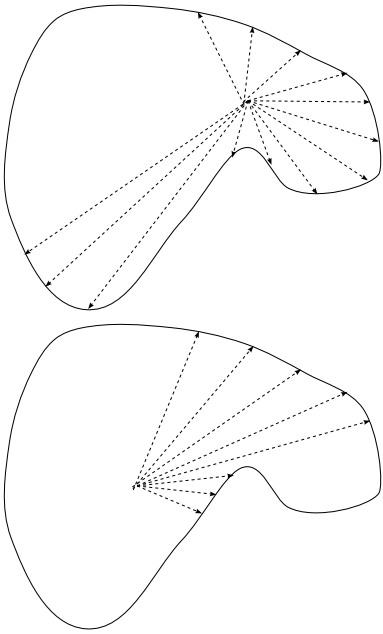

Fig. 3. Ray casting origin location for concave shapes

2 Heart Region Extraction for USG Simulations

The problem of ultrasound simulation has gained wide interest starting from fundamental work based on physical models [6], towards medical applications such as [7, 8]. With advent of cheap, multi-core processing the simulation algorithms have been successfully applied for GPGPU as in [9] and [10]. At the same time new simplified, but effective, processing algorithm such as [11] were proposed. Applications such as [12, 13] conform to the trend of utilizing simulations as a training tool in medicine that right now is considered a necessity [14, 15].

Simulation of Transesophageal Echocardiography commonly makes use of medical imaging collected during patient examination. A TEE simulator applies online algorithms transforming an input data set obtained in CT examination into a simulated USG image. This section discussed a ray casting based input data preprocessing method that provides a significant size reduction of the input data.

Given the physical properties of the USG imaging, the input needs to contain only the heart image and the position of the esophagus. Neighboring organs can be discarded without losing the educational value of the program. A raw data set of size 1-2GB is common for CT scans of a chest. Inclusion of temporal information, so that depiction of heat's cycle is possible, increases it's size significantly. Reduction of the input set size enables latency and processing limited applications to gain wider use.

The authors propose a ray-casting based method for segmentation of CT scan image and *Region of Interest* (ROI) extraction for the purpose of TEE simulation [16]. The method is based on generation of ROI mask for each of the relevant images in the input data set. The next step is superpositioning of all the masks, so that an aggregate mask enclosing all identified ROIs is obtained. The aggregation step allows for generating a 3D volume that is effectively encloses only the data that is relevant for the simulation process. The process is shown in Fig. 4.

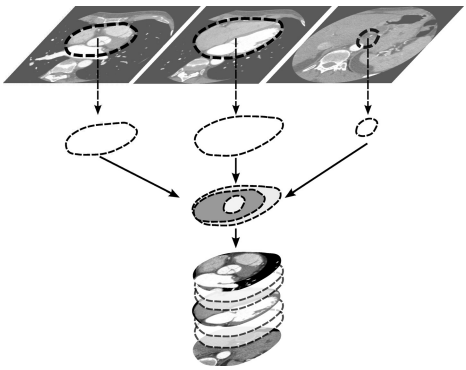

Fig. 4. Processing pipeline - segmentation of CT scan series, preparation of aggregate mask, ROI volume extraction

The concept for heart image segmentation is presented in Fig. 5. The threshold condition for ray propagation is set such that the ray should stop at the pericardium.

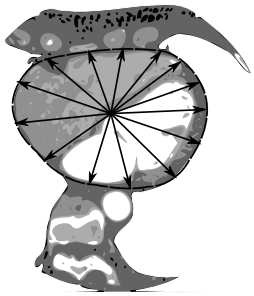

Fig. 5. Heart muscle outline using ray casting

A simple heuristic is used for selection of the origin point based on locating the center of mass of the image. Presence of contrast agent results in areas filled by blood exhibiting higher pixel values in CT images. Heart structures - ventricles,

atria, muscle tissue are thus well visible. Given that, the center of mass will be found inside the area enclosed by heart. The resulting position for 2 samples is shown in Fig. 6.

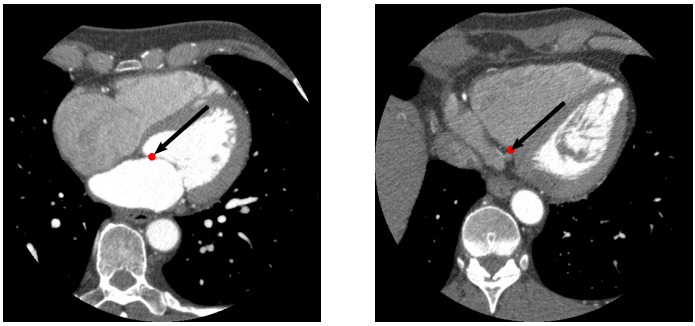

Fig. 6. Ray origin positioning

The threshold value for attenuation was empirically found to be $20HU$ and roughly corresponds to the values expected for area occupied muscle tissue. The value was confirmed by examining a number of data sets, however all images were obtained using the same CT device. The authors strongly suggest to perform additional verification and examine data collected using a particular CT scanner. The Hounsfield value is converted to pixel brightness based on metadata stored in DICOM [17, 18]. Lower values indicate lower measured attenuation, most likely the ray has entered pericardial cavity or lungs.

The result of ray casting is shown in Figure 7(b). One can clearly observe that at the sides, most of the rays stopped at pericardium, mainly due to the large difference in pixel intensity, and thus attenuation, between lungs and heart. However in anterior and posterior regions, the rays propagated farther than desired.

The boundary condition may not be met as the intensity level at the position where the ray propagation should cease is higher than expected. This may be caused by too large ray increase step, amplified by deficiency of the imaging method or existence tissue with similar properties in direct neighborhood. This problem of *mask leakage* can be limited by post processing ray casting points.

The heart can be considered to have a smooth surface, hence any abrupt changes in ray length are improbable and indicate mask leakage. The problem is displayed in Fig. 8. Significant change in ray length is visible both at the center and at the edges of the graph correspond to rays propagating towards ribs at the top and towards aorta at the bottom in Fig. 7(b). Application of a median filter with empirically selected window length alleviates the problem. The resulting ray lengths are shown in Fig. 8 using dashed line. The final shape of the mask obtained in segmentation process is displayed in Fig. 7(c).

Evaluation has been performed by verifying if the resulting masks completely enclose outlines of most significant heart regions (ventricles, atria, pericardium).

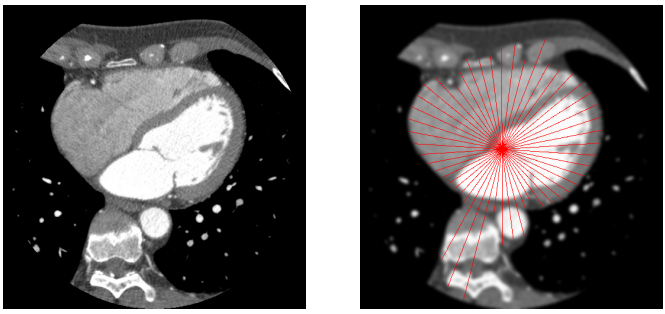

(a) Original image (b) Ray casting

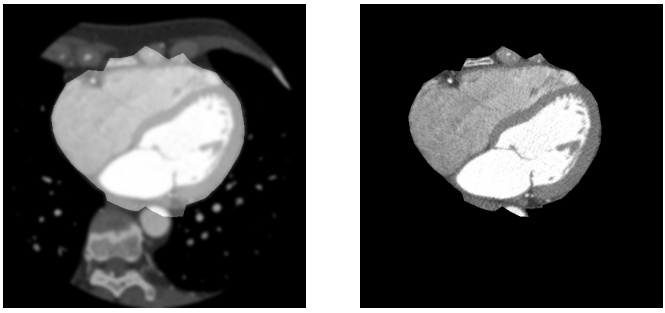

(c) Mask after ray filtering (d) Masked input image

Fig. 7. Segmentation using ray casting

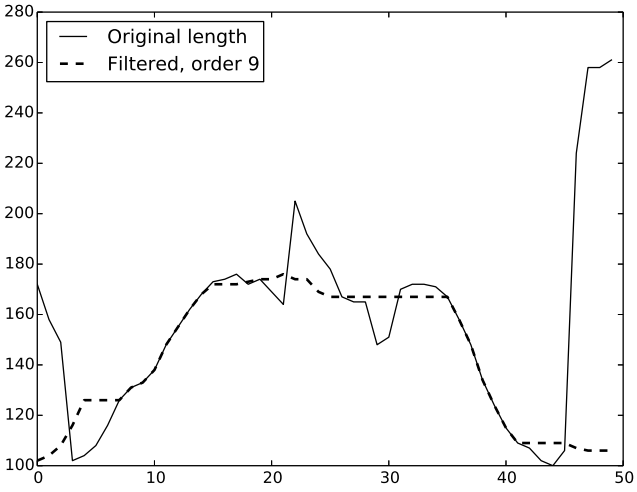

Fig. 8. Consecutive ray lengths from Fig. 7(b) (starting at bottom center, counter-clockwise), before and after filtering

For this purpose a test data with an outline of heart muscle was prepared. The obtained segmentation masks, were then verified to completely contain the reference regions. The graph showing comparison of the obtained mask to the reference area is shown in Fig. 9.

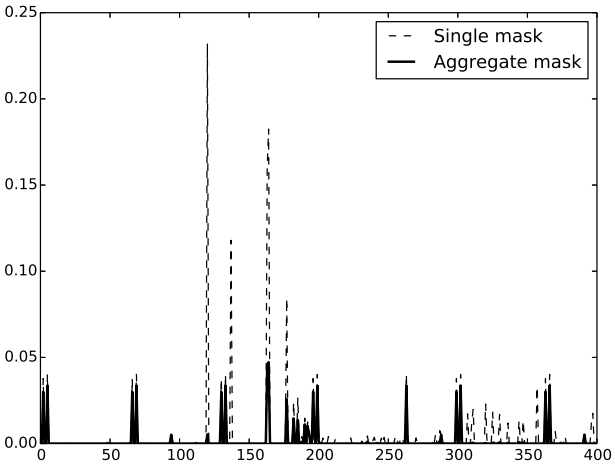

Fig. 9. Measured reference area not included in the mask, relative to mask size

There is a clear difference between the results for individual mask and an aggregate mask. Clearly, single masks have disadvantage in case the ray casting process failed to perform segmentation correctly. However, as assumed previously, the effect is compensated by use of aggregate mask. For all of reference samples, the missing area is below 5% of the mask size. Further analysis revealed that the missing area is at the edge of pericardium and does not impede the final outcome of the segmentation process. It may be expected that inclusion of a dilation step will yield an improvement and cover the missing regions.

After compression the original data set size has been reduced by factor of 18. Further steps that employed ray casting for image segmentation and extraction of the region of interest resulted in another size reduction by a factor of 2.5. Thus a single slice stored in 16-bit PNG format has been downsized to 50kB of data. At the same time the region that needs to be processed during the simulation pass has been marked and reduced significantly, as the relative area occupied by the heart is at most, less than 40% of a single horizontal slice.

3 Automated Identification of Left Ventricle Characteristic Points

Fusion of medical data is a widely regarded practice that aims at improving the diagnostic value individual imaging methods by providing a combined interpretation, thereby revealing indirectly visible aspects of the medical data.

Fusion of morphological data obtained in CT and functional information from SPECT (perfusion at rest and stress) allows for comprehensive evaluation of location and severity of ischemia, thereby increasing the diagnostic and prognostic value of noninvasive imaging techniques [19, 20].

Another application of ray casting plays a significant step in a fusion of ECHO AFI (Automated Function Imaging) [21] output with a 3D model of LV[22]. Combination of a bull's-eye representation of LV [23] stretched on a 3D mesh extracted from a series of CTA (CT Angiography) scans is vital from diagnostic point of view. The method may lower the need for performing classical, invasive angiography or can augment the analysis and interpretation of unclear CTA results. The result of the fusion process is presented in a single view, where the measured LV function is correlated spatially with a 3D model of LV [22].

Successful fusion requires knowledge of characteristic points on the left ventricle that allow for proper positioning of the bull's-eye diagram as a texture. Given the spatial reference of bull's-eye diagram, at least three distinct points need to be found on a 3D mesh. Apex and two additional points at the base of LV, near interventricular septum, were identified as sufficient, see Figure 10.

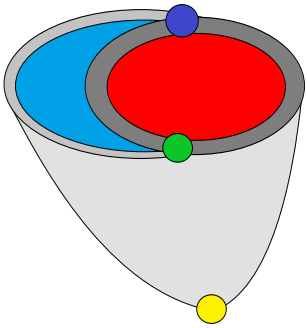

Fig. 10. Characteristic points of left ventricle: apex, two points at the base, near interventricular septum

A 3D mesh, automatically extracted by CT software does not directly contain the required information. The authors propose a ray-casting based method for location of two characteristic points at the base of LV, both points marked in Figure 10 with blue and green markers.

Each of the points if found by evaluating the conditions that refer to the locality of certain features in the 3D mesh.

The blue marker is found by iteratively casting rays, while rotating towards the back of the heart, and measuring distance between pericardium and LV wall. With each iteration, the distance is compared with previous value. Conducted analysis showed that at least 25% increase in distance is a sufficient estimate. Once, the condition has been met, the characteristic point is known to be located at the previous ray position.

The green marker is found using a similar approach. However, the distance is measured between the wall of LV and aortic sinus. The point of interest is located on the ray for which distance measurement was the smallest.

The concept is visualized in Figure 11.

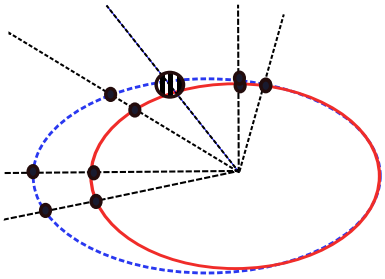

Fig. 11. Locating points of interest (marked with dashed circle) using ray casting

Presented implementations of modified ray-casting method for tracking LV anatomical points of interest provide the opportunity to define a constellation of markers essential for the images fusion performance, presented on Fig. 12.

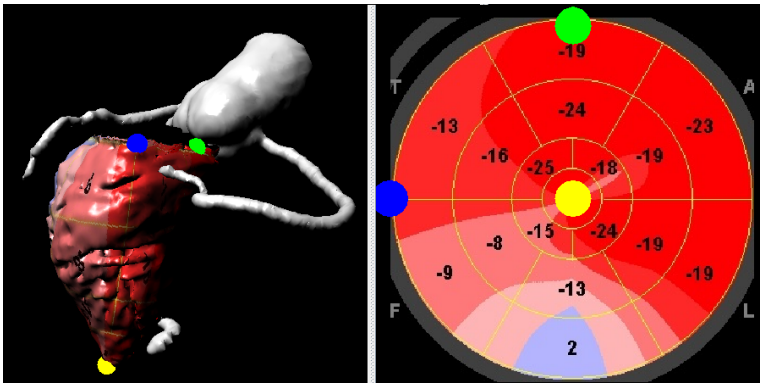

Fig. 12. Fusion of 3D model of LV with ECHO

4 Improvements

While ray casting as algorithm do not provide room for improvement, the respective implementations can be enhanced for greater performance. The algorithm may be easily extended to support a multi-threaded implementation. An inherent data level parallelism allows for work partitioning at the input image level. Lack of dependency between respective rays, allow an approach like in Fig. 13.

The profiling analysis revealed that a large portion of execution time is spent in the process of ray casting, with only little time allocated to ray length filtering, which is a sequential process. Thus, according to Amdahl's law [24, 25], splitting of ray casting task between a number of threads should yield a considerable speedup.

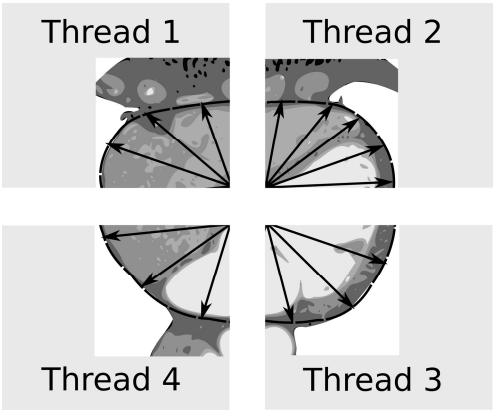

Fig. 13. Parallel ray casting implementation

Another improvement that is possible to apply is to exploit the aliasing effect of the ray propagation near the origin. The input image, as indicated in the introductory section, has a limited resolution. If a large number of rays is used, each ray will, at least for a certain length, starting from the origin, trace the same path as it's neighbors. The authors propose a use of a look-up table, addressed by coordinates of each pixel. The table would hold a binary flag indicating if a pixel was already claimed by a ray. Since all rays are checked against the same boundary condition, the flag allows for pixels that were already tested to be skipped.

5 Conclusions

The authors have presented two successful applications of ray casting for processing of medical imaging data. Although the core method is well known, it's application and enhancements proposed by authors bring a deal of novelty.

Application of ray casting in the segmentation process, although already providing good results, still needs some improvement. It has been observed that for certain samples, not all of the reference area is included within the segmentation mask. Especially at points where transition between pericardium to lungs appears, the segmentation process may partially fail, with ray not propagating far enough. It is expected that the problem can be easily addressed with a dilation step, however this would result in unnecessary increase of the whole mask.

Ray casting implementation for locating characteristic points of LV is a part of software package for supporting CAD (coronary artery disease) diagnosis. Purpose of presented algorithm is to prepare mapping for final texturing step in a fully automated manner. Should the algorithm fail or yield inadequate results, the operator has a possibility to move the markers freely, using the found positions as starting points. Tests in clinical environment using non-pathologic samples are in progress and show promising results. Still the authors have not yet verified the performance of the algorithm in case the input data set contains anomalies such as hypertrophy of the left ventricular wall.

References

1. Bowman, D.A., Hodges, L.F.: An evaluation of techniques for grabbing and manipulating remote objects in immersive virtual environments. In: Proceedings of The 1997 Symposium on Interactive 3D Graphics, I3D 1997, pp. 35–38. ACM, New York (1997)
2. Myszkowski, K., Okunev, O., Kunii, T.: Fast collision detection between complex solids using rasterizing graphics hardware. The Visual Computer 11(9), 497–511 (1995)
3. Moltz, J.H., Bornemann, L., Kuhnigk, J.M., Dicken, V., Peitgen, E., Meier, S., Bolte, H., Fabel, M., Bauknecht, H.C., Hittinger, M., et al.: Advanced segmentation techniques for lung nodules, liver metastases, and enlarged lymph nodes in CT scans. IEEE Journal of Selected Topics in Signal Processing 3(1), 122–134 (2009)
4. Bomans, M., Hohne, K.H., Tiede, U., Riemer, M.: 3-D segmentation of MR images of the head for 3-D display. IEEE Transactions on Medical Imaging 9(2), 177–183 (1990)
5. Dobkin, D.P., Wilks, A.R., Levy, S.V.F., Thurston, W.P.: Contour tracing by piecewise linear approximations. ACM Trans. Graph. 9(4), 389–423 (1990)
6. Jensen, J.A.: Simulation of advanced ultrasound systems using Field II. In: IEEE International Symposium on Biomedical Imaging: Nano to Macro, pp. 636–639. IEEE (2004)
7. Shams, R., Hartley, R.I., Navab, N.: Real-time simulation of medical ultrasound from CT images. In: Metaxas, D., Axel, L., Fichtinger, G., Székely, G. (eds.) MICCAI 2008, Part II. LNCS, vol. 5242, pp. 734–741. Springer, Heidelberg (2008)
8. Sun, B., McKenzie, F.: Real-time sonography simulation for medical training. International Journal of Education and Information Technologies 5(3), 328–335 (2011)
9. Kutter, O., Shams, R., Navab, N.: Visualization and GPU-accelerated simulation of medical ultrasound from CT images. Computer Methods and Programs in Biomedicine 94(3), 250–266 (2009)
10. Burger, B., Bettinghausen, S., Radle, M., Hesser, J.: Real-time GPU-based ultrasound simulation using deformable mesh models. IEEE Transactions on Medical Imaging 32(3), 609–618 (2013)
11. Piórkowski, A., Kempny, A.: The Transesophageal Echocardiography simulator based on Computed Tomography images. IEEE Trans. Biomed. Engineering 60(2), 292–299 (2013)
12. Goksel, O., Salcudean, S.E.: B-mode ultrasound image simulation in deformable 3-D medium. IEEE Transactions on Medical Imaging 28(11), 1657–1669 (2009)

13. Piórkowski, A., Werewka, J.: A concept of eTraining platform for cardiology learning based on SOA paradigm. In: Maciaszek, L.A., Cuzzocrea, A., Cordeiro, J. (eds.) ICEIS (3), vol. 3, pp. 261–264. SciTePress (2012)
14. Kunkler, K.: The role of medical simulation: an overview. The International Journal of Medical Robotics and Computer Assisted Surgery 2(3), 203–210 (2006)
15. Amitai, Z., Small, S.D., Wolpe, P.R.: Patient safety and simulation-based medical education. Medical Teacher 22(5), 489–495 (2000)
16. Borzęcki, M., Skurski, A., Balcerzak, B., Kamiński, M., Napieralski, A., Kasprzak, J., Lipiec, P.: Computed Tomography image processing for diagnostic and training applications in medicine. Journal of Medical Informatics and Technologies 19, 67–73 (2012)
17. Clunie, D.A.: DICOM structured reporting. PixelMed Publishing (2000)
18. Bidgood, W.D., Horii, S.C., Prior, F.W., Van Syckle, D.E.: Understanding and using DICOM, the data interchange standard for biomedical imaging. Journal of the American Medical Informatics Association 4(3), 199–212 (1997)
19. Gaemperli, O., Schepis, T., Valenta, I., Husmann, L., Scheffel, H., Duerst, V., Eberli, F.R., Luscher, T.F., Alkadhi, H., Kaufmann, P.A.: Cardiac image fusion from stand-alone SPECT and CT: clinical experience. Journal of Nuclear Medicine 48(5), 696–703 (2007)
20. Gaemperli, O., Bengel, F.M., Kaufmann, P.A.: Cardiac hybrid imaging. European Heart Journal 32(17), 2100–2108 (2011)
21. Belghiti, H., Brette, S., Lafitte, S., Reant, P., Picard, F., Serri, K., Lafitte, M., Courregelongue, M., Dos Santos, P., Douard, H., et al.: Automated function imaging: a new operator-independent strain method for assessing left ventricular function. Archives of Cardiovascular Diseases 101(3), 163–169 (2008)
22. Skurski, A., Borzęcki, M., Balcerzak, B., Kamiński, M., Napieralski, A., Kasprzak, J., Lipiec, P.: Image processing methods for diagnostic and simulation applications in cardiology. International Journal of Microelectronics and Computer Science 3(4), 146–151 (2012)
23. Murta Jr., L., Pazin-Filho, A., Schmidt, A., Almeida-Filho, O., Marin-Neto, J., Maciel, B.: Segmental quantitative analysis of myocardial contrast echocardiography images using a bullseye representation. In: Computers in Cardiology, pp. 177–180. IEEE (2003)
24. Amdahl, G.M.: Validity of the single processor approach to achieving large scale computing capabilities. In: Proceedings of the Spring Joint Computer Conference, April 18-20, pp. 483–485. ACM (1967)
25. Lee, V.W., Kim, C., Chhugani, J., Deisher, M., Kim, D., Nguyen, A.D., Satish, N., Smelyanskiy, M., Chennupaty, S., Hammarlund, P., et al.: Debunking the 100X GPU vs. CPU myth: an evaluation of throughput computing on CPU and GPU. In: ACM SIGARCH Computer Architecture News, vol. 38, pp. 451–460. ACM (2010)

A New Aortic Aneurysm CT Series Registration Algorithm

Joanna Czajkowska[1,2], Christian Feinen[2], Marcin Grzegorzek[2], Matthias Raspe[3], and Ralph Wickenhöfer[4]

[1] Silesian University of Technology, Faculty of Biomedical Engineering, Department of Informatics and Medical Equipment, Zabrze, Poland
[2] University of Siegen, Institute for Vision and Graphics, Research Group for Pattern Recognition, Siegen, Germany
[3] SOVAmed GmbH, Koblenz, Germany
[4] Herz-Jesu-Krankenhaus, Dernbach, Germany
joanna.czajkowska@polsl.pl

Abstract. Nowadays, vascular diseases are the most challenging health problems in developed countries. Despite the fast development of modern contrast-enhanced Computed Tomography (CT), providing complex 3D datasets, the tremendous amount of problems still remain unsolved. The vascular segmentation as well as registration techniques are the topics of past and on-going research activities. In this work we focus on an abdominal aortic aneurysm registration technique. The developed approach makes it possible to match all voxels belonging to the aorta from pre- and post-operative CT data. The presented technique is based on aorta lumen segmentation and graph matching method. To segment the lumen area a hybrid level-set active contour approach is used. The matching step is performed based on a path similarity skeleton graph matching procedure. The registration results have been tested on the database of 8 patients, for which two different contrast-enhanced CT series were acquired. All registration results achieved with our system and verified by an expert prove the efficiency of the approach and encourage to further develop this method.

Keywords: Hybrid Level-Set Active Contour, Graph Matching, Image Registration, Skeletonization.

1 Introduction

Nowadays, vascular diseases belong to the most challenging health problems in developed countries. An abdominal aortic aneurysm (AAA), addressed in our approach, is a dilated and weakened segment of the abdominal aorta. It is an abnormal ballooning of the abdominal portion of the aorta, that occurs as a consequence of aortic medial degeneration and can break open causing death. An AAA can develop in anyone, however it is mostly seen in males over 60, having one or more risk factors. During last 30 years, the occurrence of AAA has increased threefold. To prevent from rupturing, interventional radiologists offer

E. Pietka, J. Kawa, and W. Wieclawek (eds.), *Information Technologies in Biomedicine, Volume 3*, Advances in Intelligent Systems and Computing 283,
DOI: 10.1007/978-3-319-06593-9_2,

minimally invasive treatment for abdominal aortic aneurysm, which is specially important when it reaches 5 centimeters in diameter. Currently, there are different AAA treatment options. The open surgical repair by a vascular surgeon is the most commonly used for a large, unruptured aneurysm. The less invasive and relatively new technique, eliminating the need for a large abdominal incision, is placing a graft within the aneurysm. It redirects blood flow and stops direct pressure from being exerted on the weak aortic wall [2, 1]. An exemplary 3D volume rendering of CTA series of pre- and post-operative study created using Osirix software is shown in Fig. 1.

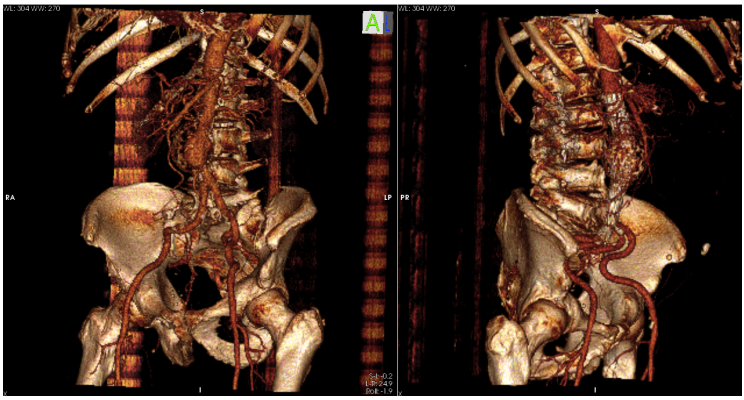

Fig. 1. 3D volume rendering of CTA series of pre- (left) and post-operative (right) study of aortic aneurysm provided by Osirix software

The AAA is mostly diagnosed by a physical examination as a soft mass in the abdomen. For more accurate and efficient diagnosis the development of imaging techniques provides numerous tools used to examine vessels and display their details. A contrast-enhanced CT angiography (CTA), which replaced a conventional angiogram, is an imaging technique commonly used in vascular diagnosis. Despite the fast development of modern contrast-enhanced Computed Tomography (CT), providing complex 3D datasets, the tremendous amount of problems still remain unsolved. The vascular segmentation [3] and registration techniques are the topics of past as well as on-going research activities.

From the medical background of AAA, two region of interests: aorta lumen and thrombus, can be defined. An exemplary manual segmentation results of both of them in a CT scan are shown in Fig. 2. The newest approaches in AAA segmentation [3, 5, 6] address either both of the problems or only a chosen one. An automated method for the segmentation of thrombus in abdominal aortic aneurysms from CTA data is presented in [5]. The Active Shape Model (ASM) fitting is performed in sequential slices. As the starting point for the analysis the results obtained for the adjacent slice are used. The full 3D segmentation technique in CTA is reported in [6]. The system analyses both global features,

incorporating a priori knowledge of the intensity, volume, and shape of the aorta and other structures, and the local information like voxel location, intensity, and texture information. All of them are used for training and driving a support vector machine classifier. As reported in [3] the current state of the art in AAA segmentation is modelling, feature analysis or their combination, and in all these areas different efficient techniques can be found. However, the authors also claim, that there are some problems, which still remain unsolved. There is no standardly accepted databases and validation criteria for most vascular segmentation applications and the direct performance comparisons of the segmentation results have not been performed yet.

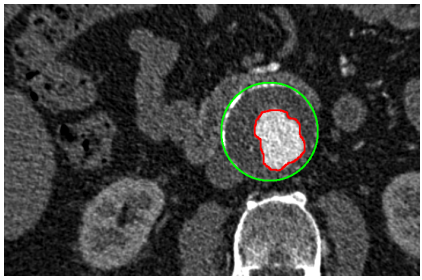

Fig. 2. An example of an contrast-enhanced CT scan of an abdominal aortic aneurysm with segmented thrombus (outer green contour) and lumen (inner red contour)

Despite the fact that the segmentation of vascular structures is valuable for diagnosis assistance, treatment and surgery planning the currently developed computer aided diagnosis (CAD) software target in efficient image registration. It does not only allow measurements of lumen or thrombus volume, but combining different image information is also useful for treatment planning and monitoring. Thanks to it, the comparative analysis of consecutive (pre- and post-operative) CTA studies as well as matching of different image modalities is possible.

Depending on the application, various registration techniques have been reported [7–11]. The registration methods, which address the problem of simultaneous analysis of different image modalities are given in [7–10], whereas the pre- and post-operative CTA sequence matching algorithm is presented in [11]. The authors of [9] propose a registration technique based on the overlaying the preoperative 3D model of the aorta onto the intraoperative 2D X-ray images. The presented technique utilizes two X-ray images showing the abdominal aorta from different angles in an integrated way. They developed a hierarchical registration scheme deployed by a sensible partition of the registration parameter space based on the image acquisition protocol and the patients motion constraint.

The 2D/3D registration technique is also addressed in [7]. The non-rigid method enables information from the CT to be overlaid onto the fluoroscopy images during the implantation procedure. The authors have investigated the

use of manually picked landmarks and the thin plate spline algorithm to deform the CT surface so it more accurately represents the interventional scene. The automatic movement compensation in 2D/3D registration of fluoroscopy and preoperative volumetric data is presented in [10]. The paper proposes a pelvis boundary detection method that enables real time monitoring of patient movement and an automatic 2D/3D re-registration algorithm that compensates for it.

The idea of a graph-based approach in this context is presented in [8]. The introduced 2D/3D registration method is there formulated on a 3D graph and applied for AAA interventions. As an input, the algorithm takes the 3D graph generated from a segmentation of the CT volume and the 2D distance map calculated from the 2D X-ray image. For computing the graph similarity, different measures are then used in a length preservation and a smoothness regularization term.

In this work we focus on 3D abdominal aortic aneurysm registration technique. The developed approach makes it possible to match the aorta segmented in pre- and post-operative CTA data. The presented technique is based on an aorta lumen segmentation and graph matching technique. In the segmentation step a hybrid level-set active contour approach is employed. The applied hybrid medical image segmentation method in the level-set framework [12] uses the object's boundary as well as region information. In this approach a boundary gives the information concerning object location, whereas the region features help to avoid the boundary leakage. The matching step is performed based on a path similarity skeleton graph matching procedure introduced in [21].

In the following section, a short introduction to the hybrid active contour approach [12] applied for AAA lumen segmentation is given. In Section 3, the 3D skeletonization algorithm for graph extraction is described. Section 4 introduces the graph matching technique and Section 5 presents the experiments and the obtained results. Then, the last section (Section 6) concludes the work and outlines plans for the future.

2 Abdominal Aortic Aneurysm Segmentation Method

The active contour model for image segmentation was originally developed by Kass at. all [13] and the energy minimization techniques in image segmentation have attracted researches in the last two decades. The basic idea of the snake method [13] is to iteratively evolve the initial contour towards the regions described by some certain features. The movement of the energy minimizing-spline is guided by the geometry of the evolving curve (internal force) and influenced by image features (external force). The image information pull the contour into the lines, edges or terminations. Local minima of the contour energy correspond to desired image properties. Since the classical implementation of the snake method [13] was introduced, different modifications and improvements dictated by its new applications were incorporated. Active contour model expanded by gradient vector flow is presented in [14]. This efficient algorithm remains limited

to the segmentation of structures with well defined contours. Geodesic active contour model [15] and Chan-Vese approach [16] are two most important techniques improving this segmentation technique standing out for boundary-based and region-based methods.

In all the cases mentioned above, the image segmentation methods are based on minimizing a predefined energy functionals. To solve the curve evolution partial differential equations (PDEs) different numerical methods are applied. In a classical approach the finite set of contour points approximates the parametric contour $\Psi(s) = (x(s), y(s)),\ s \in [0,1]$ and the contour changes in time $\Psi(s,t) = (x(s,t), y(s,t)),\ s \in [0,1], t = \mathbf{R}_+ \cup \{0\}$ - the contour evolves with the points movement. Geodesic [15], Chan-Vese [16] and the hybrid active contour [12] used in this paper belong to the models developed in a level-set framework. In the implementation [15] the solution of the particular energy snakes model is given by a geodesic curve in a Riemannian space, being induced form the image. The Chan-Vese active contour model [16] is based on the mean curvature motion. The curve C is implicitly represented via a Lipschitz function ϕ and by $mathitC = \{(x,y)|\phi(x,y) = 0\}$. The initial contour is defined by the set $\{(x,y)|\phi_0(x,y) = 0\}$ and the evolution of the curve is given by the zero-level curve at time t of the function $\phi(t,x,y)$. To solve the PDE the curve C evolves in normal directions with the speed F [16]

$$\frac{\partial \phi}{\partial t} = |\nabla \phi| F, \phi(0,x,y) = \phi_0(x,y). \tag{1}$$

2.1 Hybrid Level-Set Method

The same as in the active contour given in [16] in the hybrid technique [12], employed in our work, the active contour C is represented by the zero set of embedding function ϕ, such that $C = \{x|\phi(x) = 0\}$. The points inside and outside the contour have positive and negative ϕ values, respectively. The minimized functional in image I domain Ω is defined as

$$E(\phi) = -\alpha \int_\Omega (I - \mu) H(\phi) d\Omega + \beta \int_\Omega g |\nabla H(\phi)| d\Omega, \tag{2}$$

where $g = g(|\nabla I|)$ is a boundary feature map related to the image gradient. The parameters α and β balance the two terms of (2), and μ indicates the lower bound of the gray-level of the target object. Thanks to it, the curve evolves to enclose the regions greater than μ. The PDE of the functional (2) is derived from the Gateaux derivative gradient flow [12]

$$\phi_t = |\nabla \phi| \left[\alpha (I - \mu) + \beta div \left(g \frac{\nabla \phi}{|\nabla \phi|} \right) \right], \tag{3}$$

and the explicit curve evolution PDE is represented by [12]

$$C_t = \alpha (I - \mu) \overrightarrow{N} - \beta \langle \nabla g \cdot \overrightarrow{N} \rangle \overrightarrow{N} + \beta g \kappa \overrightarrow{N}. \tag{4}$$

The direction of the curve normal $\overrightarrow{N}$ is defined to point outward the curve and $\overrightarrow{N} = -\frac{\nabla\phi}{|\nabla\phi|}$. The curvature κ is given by $\kappa = div\left(\frac{\nabla\phi}{|\nabla\phi|}\right)$. The used iterative curve evolution algorithm, based on additive operator splitting (AOS) approach is in detail described in [12]. Some preprocessing steps and parameter set up are described in Sections 2.2 and 5, respectively.

2.2 Preprocessing and Initial Surface Selection

The analysed CTA series are affected by artefacts and noise, which can influence the final segmentation results. Therefore, as a preprocessing step a 3D adaptive filtering procedure was employed. The selected filtering technique based on anisotropic diffusion [18] increases the Signal-to-Noise Ratio (SNR) and preserves the edges.

In the hybrid level-set implementation applied to volumetric CT data, the authors of [12] used a sphere as an initial surface. The results presented by them show that it successfully converges to the target object. However, the performed experiments proved, that the time to converge the hybrid level-set algorithm [12] strongly depends on this surface. In our work, the size of the analysed AAA CTA data ($512 \times 512 \times n$, where $n \in [220, 680]$) determined the clustering-based initial surface selection procedure. For this, we used a weighted fuzzy c-means clustering procedure introduced in [17]. The initial surface was then created by all the voxels belonging to the cluster with the highest mean gray intensity value.

Thanks to this two preprocessing techniques the hybrid level-set algorithm enables fast and robust AAA segmentation. An exemplary final 3D segmentation results of abdominal aorta lumen in CT series are shown in Fig. 3.

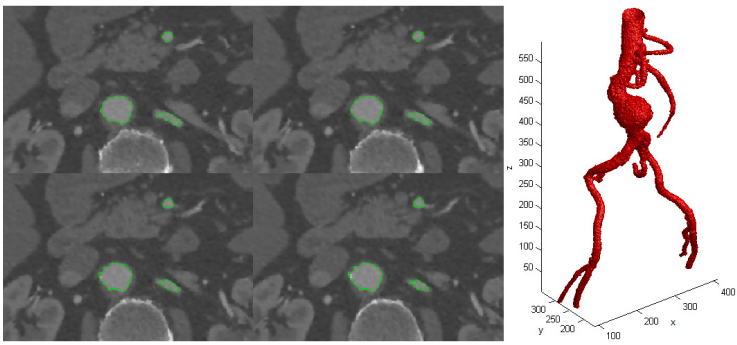

Fig. 3. An example of 3D abdominal aorta lumen segmentation results in an image view (left) and volume rendering (right)

3 Skeletonization

The CTA volume matching procedure being an overall goal of our work is based on graph matching step described in the next section. For this a 3D skeletonization step is incorporated. The 3D skeleton is obtained using the method described in [19]. This automatic algorithm computes subvoxel precise skeleton of volumetric data based on subvoxel precise distance field. The advantage of the subvoxel approach over a voxel precise skeleton is, that it computes an accurate, more precise and centered skeleton also for objects that are less than a single voxel thick. The authors of [19] have proven, that it is a proper solution for the accurate measurements of the object, such as vessel cross section or volume.

The input for the skeletonization method described in [19] is a subvoxel precise distance field. To obtain this field the authors suggest a two steps preprocessing technique. First, a level set time-crossing map calculation followed by a distance field computation is performed. Then, a sampled level set time-crossing map with the embedded zero-crossing isosurface is estimated. In our approach, the isosurface required for this, which yields the object's true boundary is created based on the previously obtained segmentation results. Having a implicit representation of the boundary, we estimate the subvoxel precise Euclidean distance transform for n-dimensional data [20].

The Euclidean distance field is then used to find the point with the largest distance from the boundary and to determine a speed image used as an input for the fast matching propagation step. The speed image being a function of the distance field (d - distance value and D - maximum distance value)

$$v = \left(\frac{d}{D}\right)^2 \tag{5}$$

is used to determine the curve evolution velocity for each pixel. The point at the global maximum distance from the objects boundary is calculated in a single pass through the distance field. The first one encountered in scanline order is used in the situation, if no unique maximum point exists. It is a start point for a fast marching propagation algorithm, in which the obtained speed image is used. The fast marching propagation is augmented to calculate the geodesic distance (Manhattan distance) inside the object starting at the global maximum point of the distance field. Based on the obtained results the branch points are then estimated. The furthest point of the model from the global maximum distance point is used as the start point of the branch. The remaining points of the branch are determined by performing a gradient descent, back-tracking procedure on the fast marching time-crossing map. This process is repeated for each branch of the created skeleton [20]. The exemplary results of application of this method to AAA data are shown in Fig. 4.

4 Graph Matching

The previously obtained aorta skeletons are now matched to properly register the two analysed 3D CTA series for each examination. The registration procedure

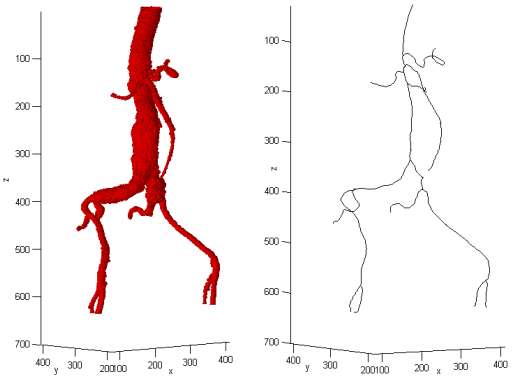

Fig. 4. An exemplary result of applying 3D skeletonization procedure (right) to an abdominal aorta surface (left)

we used is based on the algorithm presented in [21]. In contrast to existing approaches to skeleton similarity, the main idea of this approach is to match the skeleton graphs by comparing the geodesic paths between their endpoints. Therefore, the authors do not explicitly consider the topological structure of the skeleton trees or graphs.

According to the definition given in [21] the so called skeleton path is "a shortest path between a pair of end nodes on a skeleton graph". Based on the previously obtained segmentation and skeletonization results, and using a distance transform $DT(t)$ we are able to approximate the radius $R_{m,n}(t)$ of the maximum disk at each skeleton point with index t in a skeleton path $p(v_m, v_n)$ connecting the end nodes v_m and v_n. Therefore, the path is sampled by K equidistantly distributed points. Due to the fact, that the CTA series also differ in the voxel size, the normalization term proposed in [21] making the method invariant to the scale is also required.

To define the similarity/dissimilarity between two skeleton paths R and R' the authors of [21] suggest a path distance measure as

$$p_d(p(u,v), p(u',v')) = \sum_{i=1}^{M} \frac{(r_i - r'_i)^2}{r_i + r'_i} + \alpha \frac{(l - l')^2}{l + l'}, \tag{6}$$

where l and l' are the lengths of paths $p(u,v)$ and $p(u',v')$ and α is a weighting factor.

Let the two CTA series be described by two ordered graphs G and G' with $K+1$ and $N+1$ nodes ($K \leq N$) respectively. The matching cost $c(v_i, v'_j)$ between end nodes v_i and v'_j is estimated based on the paths to all other vertices in G and G' that emanate from v_i and v'_j. The dissimilarity value between the end nodes is estimated using the optimal subsequence bijection (OSB) method introduced in [24]. The advantage of the OSB algorithm is, that it finds a subsequence a' in sequence a that best matches b' in b skipping possible outlier elements. To prevent

from skipping too many elements of sequence a the authors of [21] suggest a penalty term b_∞, being an additional element of b. The distance function d computes the dissimilarity between a and b, that is, $d(a_i, b_j)$ is given for all $(i, j) \in \{1, \ldots, m\} \times \{1, \ldots, n, \infty\}$, where m and n stand for the length of a and b, respectively. As distance function d the path distance p_d, defined in (6), is used. The distance to the additional element $d(a_i, b_\infty)$ is a constant for all $i \in \{1, \ldots, m\}$ determining the cost of skipping any given element on the sequence a. The so called "jumpcost" j_c is computed as

$$j_c = \mu + \sqrt{\frac{1}{m} \min_{j=1,\ldots,n} (d(a_i, b_j) - \mu)^2}, \quad \mu = \sum_{i=1}^{m} \frac{1}{m} \min_{j=1,\ldots,n} (d(a_i, b_j)). \tag{7}$$

Then, for any given correspondence, the distance between two sequences is defined in [21]

$$d(a, b, f) = \frac{1}{m} \sum_{i=1}^{m} (d(a_i), b_{f(i)})^2. \tag{8}$$

Therefore, an optimal correspondence $\widehat{f}$ of elements in the sequence a to elements in the sequence b over all possible correspondences f is defined as

$$\widehat{f} = arg \min\{d(a, b, f)\}. \tag{9}$$

The optimal correspondence is found with the shortest path algorithm on a directed acyclic graph (DAG), in detail described in [21].

The already described OSB is applied to the matrix of the path distances between the two sequences $v_{i0}, v_{i1}, \ldots, v_{iK}$ in G ($v_i = v_{i0}$) and $v_{j0}, v_{j1}, \ldots, v_{jN}$ in G' ($v_j = v_{j0}$). For the two analysed graphs G and G' all the dissimilarity costs between their end nodes are estimated and stored in a matrix $C(G, G')$. The total dissimilarity $c(G, G')$ between G and G' computed in [21] with the Hungarian algorithm on $C(G, G')$ is here replaced by the algorithm proposed in [23]. The authors presented there Maximum Weight Subgraphs (MWS) which can be expressed as an integer quadratic problem:

$$\max g(\mathbf{x}) = \mathbf{x}^T A \mathbf{x} \qquad \text{subject to} \qquad \mathbf{x}^T M \mathbf{x} = 0, \quad \mathbf{x} \in [0, 1]^n, \tag{10}$$

where A is a symmetric $n \times n$ affinity matrix with $\forall i, j = 1 \ldots, n : A_{i,j} \geq 0$ and $M \in \{0, 1\}^{n \times n}$ represents a symmetric mutex matrix. The size of A corresponds to the number of feature points that have been detected and the diagonal of A is created using the output values obtained by the OSB. Since A expects similarity data, the OSB cost values have to be converted. For this, a Gaussian function with $\mu = 0.2$ and $\sigma = 10$ is used. To populate the non-diagonal elements of A, a pairwise distance consistency value is generated between two assignments.

$$A(u, v) = \exp(\frac{(d(i, j) - d(i', j'))^2}{2\sigma^2}), \tag{11}$$

where $u = (i, i')$ and $v = (j, j')$ are the two assignments, the Euclidean distance $d(i, j)$ is calculated.

The exemplary results of matching two CTA series, or more accurately their skeletons is shown in Fig. 5.

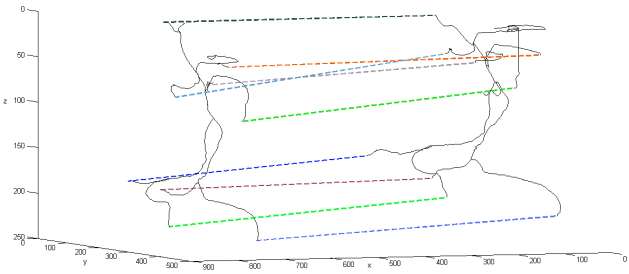

Fig. 5. The exemplary results of matching two AAA skeletons

5 Results

The presented segmentation/registration framework was tested on the database provided by the SOVAmed GmbH[1]. It consists of 8 pairs of of CTA series to be segmented and matched. The examinations contain pre- as well as post-operative data with the resolution of (512×512) and the number of slices in the volume varying form 220 to 680. In the preprocessing step, anisotropic diffusion filtering with a conduction coefficient function $q(x, y, z, t) = \frac{1}{1+\left(\frac{\nabla I}{\nu}^2\right)}$ proposed by Perona and Malik in [18] is used. The ν is the gradient modulus threshold that controls the conduction experimentally set to 70. Based on the normalized CTA data the number of clusters used in initial surface construction was set to 5. In the employed hybrid level-set segmentation technique [12], a boundary feature map related to the image gradient is a decreasing function g such as $g = \frac{1}{1-c|\nabla I|^2}$, with the constant c controlling the slope set to 5. The parameters required for (2) are set to $\alpha = 0.5$ and $\beta = 0.2$, respectively. The proposed set-up makes it possible to efficiently segment the aorta in all 16 analysed series. The obtained segmentation results were then used in a matching/registration step.

For all the analysed pairs of volumetric data the skeletonization procedure and matching algorithm were used. The proper skeletons were obtained for all the 8 pairs. All of them were then matched and the matching results were verified by an expert. As matching results, a labelled skeleton points on both the series were marked, so that the expert was able to verify them. In 4 for 8 analysed examinations the registration was correct. 4 of them required some manual improvements. However, the analysis was performed on a real dataset, not prepared for the analysis in any special way. The the difficulties in matching step were caused by a different resolution of the series as well as their different length. In all the cases, the series did not show exactly the same part of a patient body. However, the need of the manual intervention will be reduced in a future work. For this, we plan to incorporate a DICOM positioning information and modify the matching algorithm so that it will be invariant to the resolution and the length.

[1] `www.sovamed.com/en`

6 Conclusions and Future Work

The paper presents a preliminary study in a 3D registration of abdominal aortic aneurysm in CTA. The developed method consists of 3D segmentation part and graph based registration procedure. The promising results obtained for 8 examinations consisting of 2 CTA series each encourage to further develop this technique. In our work we plan to improve the segmentation as well as registration results incorporating a DICOM positioning information. One of the ideas is to use an algorithm for automatic understanding medical images presented in [22]. For future work an extended database is also considered.

Acknowledgement. This work was funded by the German Research Foundation (DFG) as part of the research training group GRK 1564 "Imaging New Modalities".

The experimental data was provided by SOVAmed GmbH.

References

1. Abdominal Aortic Aneurysm, Society of Interventional Radiology, Enhanced Care Trough Advanced Technology
2. Zarins, C.K., White, R.A., Schwarten, D., Kinney, E., Diethrich, E.B., Hodgson, K.J., et al.: AneuRx Stent Graft Versus Open Surgical Repair of Abdominal Aortic Aneurysms: Multicenter Prospective Clinical Trial. J. Vascular Surg. 29, 292–308 (1999)
3. Lesage, D., Angelini, E.D., Bloch, I., Funka-Lea, G.: A review of 3D vessel lumen segmentation techniques: Models, features and extraction schemes. Medical Image Analysis 13(6), 819–845 (2009)
4. Xiang, B., Latecki, L.J.: Path Similarity Skeleton Graph Matching. IEEE Transactions on Pattern Analysis and Machine Intelligence 30(7), 1282–1292 (2008)
5. de Bruijne, M., van Ginneken, B., Niessen, W.J., Maintz, J.B.A., Viergever, M.A.: Active-shape-model-based segmentation of abdominal aortic aneurysms in CTA images. In: Proc. SPIE 4684, Medical Imaging: Image Processing, p. 463 (May 2002)
6. Zhuge, F., Rubin Geoffrey, D., Shaohua, S., Sandy, N.: An abdominal aortic aneurysm segmentation method: Level set with region and statistical information. Medical Physics 33, 1440–1453 (2006)
7. Raheem, A., Carrell, T., Modarai, B., Penney, G.: Non-rigid 2D-3D image registration for use in endovascular repair of abdominal aortic aneurysms. In: Medical Image Understanding and Analysis, pp. 153–157 (2010)
8. Liao, R., Tan, Y., Sundar, H., Pfister, M., Kamen, A.: An Efficient Graph-Based Deformable 2D/3D Registration Algorithm with Applications for Abdominal Aortic Aneurysm Interventions. In: Liao, H., "Eddie" Edwards, P.J., Pan, X., Fan, Y., Yang, G.-Z. (eds.) MIAR 2010. LNCS, vol. 6326, pp. 561–570. Springer, Heidelberg (2010)
9. Shun, M., Liao, R., Pfister, M.: Toward smart utilization of two X-ray images for 2-D/3-D registration applied to abdominal aortic aneurysm interventions. In: 2011 4th International Conference on Biomedical Engineering and Informatics (BMEI), October 15-17, vol. 1, pp. 550–555 (2011)

10. Liang, D., Bo, D., Shun, M., Pfister, M., Rui, L.: Visual check and automatic compensation for patient movement during image-guided Abdominal Aortic Aneurysm (AAA) stenting. In: 2012 5th International Conference on Biomedical Engineering and Informatics (BMEI), October 16-18, pp. 391–394 (2012)
11. Sun, Z., Helical, C.T.: angiography of fenestrated stent grafting of abdominal aortic aneurysms. Biomed. Imaging Interv. J. 5(2) (April-June 2009)
12. Zhang, Y., Matuszewski, B.J., Shark, L.-K., Moore, C.J.: Medical Image Segmentation Using New Hybrid Level-Set Method. In: IEEE International Conference on Biomedical Visualisation, MEDi08VIS, London, pp. 71–76 (July 2008)
13. Kass, M., Witkin, A., Terzopoulos, D.: Snakes: Active contour models. International Journal of Computer Vision 1(4), 321–331 (1998)
14. Xu, C., Prince, J.L.: Snakes, shapes, and gradient vector flow. IEEE Transaction on Image Processing 7(3), 359–369 (1998)
15. Caselles, V., Kimmel, R., Sapiro, G.: On geodesic active contours. International Journal of Computer Vision 22(1), 61–79 (1997)
16. Chan, T.F., Vese, L.A.: Active contours without edges. IEEE Transactions on Image Processing 10(2), 266–277 (2001)
17. Kawa, J., Pietka, E.: Kernelized Fuzzy C-Means Method in Fast Segmentation of Demyelination Plaques in Multiple Sclerosis. In: Proceedings of the 29th Annual International Conference of the IEEE EMBS (August 2007)
18. Perona, P., Shiota, T., Malik, J.: Anisotropic Diffusion. Geometry-Driven Diffusion in Computer Vision 3, 73–92 (1994)
19. Van Uitert, R., Bitter, I.: Subvoxel precise skeletons of volumetric data based on fast marching methods. Medical Physics 34(3), 627–638 (2007)
20. Uirert, R.V., Bitter, I.: Subvoxel accurate Euclidean distance transforms for n-dimensional data (unpublished)
21. Bai, X., Latecki, L.J.: Path similarity skeleton graph matching. IEEE Transactions on Pattern Analysis and Machine Intelligence 30(4), 1282–1292 (2008)
22. Tadeusiewicz, R.: What Does It Means "Automatic Understanding of the Images?". In: IEEE International Workshop on Imaging Systems and Techniques, IST 2007, pp. 1–3 (May 2007)
23. Ma, T., Latecki, L.J.: Maximum weight cliques with mutex constraints for video object segmentation. In: IEEE CVPR, pp. 670–677. IEEE (2012)
24. Latecki, L.J., Wang, Q., Koknar-Tezel, S., Megalooikonomou, V.: Optimal Subsequence Bijection. In: ICDM, pp. 565–570 (2007)

Angular Resolution Study of Vectors Representing Subtle Spiculated Structures in Mammograms

Magdalena Jasionowska[1] and Artur Przelaskowski[2]

[1] Warsaw University of Technology, The Faculty of Electronics and Information Technology, 00-665 Warsaw, Nowowiejska 15/19, Poland
mjasiono@ire.pw.edu.pl
[2] Warsaw University of Technology, The Faculty of Mathematics and Information Science, 00-662 Warsaw, Koszykowa 75, Poland
arturp@mini.pw.edu.pl

Abstract. In this paper various multiscale transformations, such as contourlets, curvelets, tensor and complex wavelets, were examined in terms of the precise representation of texture directionality in medical images. In particular, subtle radiating and spiculated structures in mammograms were modeled with sparse vectors of the image linear expansions. Important properties of angular resolution, angular selectivity and shift invariance have been evaluated with simple phantoms. According to the experimental results, the complex wavelets have been proved to be the most effective tool in mammogram preprocessing to extract and uniquely represent relevant spicular symptoms for accurate diagnosis.

Keywords: angular resolution and selectivity, shift (rotate) invariant, multiscale transform, spiculed structures enhancement.

1 Introduction

Effective and of good quality imaging is important for further medical decision making. Radiologist interprets medical images, describing the physical components of potential visualized findings, such as shape, growth, and density tissue. Precise characteristic of observed structures or some objects in the background of imaged tissue tends to be significant issue to make an early and correct diagnosis by both radiologists and computer-aided systems. In the case of some pathological findings, for example architectural distortion in mammography, directionality of their structures (commonly called spicules) is one of the main important features to determine these pathology, observed on mammograms.

1.1 Mammographic Spicules

Architectural distortion is a breast lesion in which the normal structure of the breast parenchyma is distorted as if being pulled into a central point, without a

E. Pietka, J. Kawa, and W. Wieclawek (eds.), *Information Technologies in Biomedicine, Volume 3*, Advances in Intelligent Systems and Computing 283,
DOI: 10.1007/978-3-319-06593-9_3,

visible central density [3]. Briefly and clearly saying, it is a group of spicules radiating from a certain area – not the visible mass. In contrast to other pathological lesions in mammography, i.e. microcalcifications, oval or spiculated masses, architectural distortions are not well-defined [5]. Moreover, interpretation process of mammograms is significantly affected by image quality, conditioning of content assessment, individual radiologist knowledge and experience etc. affecting cognitive errors. Therefore, architectural distortions as a subtle ambiguous directional findings are commonly misdiagnosed even by the most experienced radiologists [21]. The only typical feature of this type of pathology in mammography is radiating spicules, but orientation distribution of these subtle mammographic structures is often not clearly defined.

From the viewpoint of image processing, a model of architectural distortion can be assumed piecewise lines propagated in different directions. Such an approach is used in many research studies on automatic recognition of this type of abnormalities on mammograms. In order to extract spicules, the analysis of local oriented edges [14, 15], statistical analysis of a map of pixel orientations [13], skeleton analysis [16] or top-hat partial reconstruction [10–12] were conducted. Moreover, the Dixon and Taylor line enhancement algorithm with a line strength map (as their result) indicated the potential presence of oriented lines [23], estimation of a mean curvature sign and the concentration index [17, 18], Gabor filtering and phase portrait [4, 20] or a curvilinear structure (CLS) ridge detection [6] were used.

Additionally, conducting image structure analysis our attention should be paid to image noise. Therefore, it is worth noting that noise of digital mammogram can be model as spatially correlated Poisson noise [1, 2, 22] and the noise power is closely related to breast tissue (glandular to adipose tissue) [19].

1.2 Spicule Representation in Adjusted Transform Domain

Because of redundancy and limited quality of source image domain, the appropriate spicule representation requires an optimally adjusted image transform domain that allows precise extraction of piecewise structures of different orientations in analyzed image. Therefore, an angular resolution and selectivity, shift (rotation) invariance seem to be decisive to identify the effective image transformation. Moreover, low transform-domain redundancy and low computational complexity play also a significant role in design of useful numerical descriptors of subtle mammographic structures with differentiated directionality. The abovementioned three major properties can be interpreted for our research as follows:

- angular resolution – the number of possible to distinguish directions in image,
- angular selectivity – the ability to distinguish between closely located objects in image (so-called angular separation),
- shift (rotation) invariant – the same image (spectrum) in transform domain independent of small shift (rotation) of objects in input image.

There are many various methods for global image analysis of texture directionality. It is possible to capture dominant orientations in a whole image using these global transformations, but it sometimes affects a noticeable number of false positives in image processing (in case of architectural distortions). Such approach associated with global directional characteristics, for instance based on 2D polar FFT, could be applied at one initial stage of recognition process to select the regions of interests (ROIs) with increased sensitivity of detection procedures [7]. However, it is realized at the expense of permissible false positives reduced at next stages based on more precise analysis of local structure directionality.

Local multiscale analysis of image texture could be adjusted to specific features of selected ROIs providing better results of spicule detection [8]. However, certain conditions should be fulfilled. First, local analysis should be matched to the scale range of real informative structures in order to enhance only image structures of interests and consequently to avoid false positives in detection process. Second, too high computational complexity, which is often accompanied by local image texture analysis (e.g. using Gabor filters [7]) as well as too high domain redundancy of complex data correlation limit achieved performance.

The main goal of research presented in this paper is to investigate the suitability of some local multiscale transformations for extraction of relevant directional structures in mammograms. For this purpose, the selected bases/frames of tensor wavelets, complex wavelets, contourlets and curvelets have been experimentally studied and verified according to criteria of representation clarity of proposed modeled multidirectional spicules.

Our attention has been paid to directional precision in determining of piecewise linear structure orientations due to improve of distributed spicule description and consequently increase of its recognition efficiency. The structures were modeled in domains of four selected multiscale image transformations which have been found to be useful for multiscale analysis of many advantageous applications. In particular, an influence of the size of clearly represented line structures, possible to distinguish the distance of close-lying structures, and the target sensitivity due to the rotation of line structures have been tested. To facilitate correct interpretation information compaction in as sparse as possible object representation in multiscale domain has been investigated.

2 Experimental Test of Angular Resolution

The angular resolution of new image domain should be matched to real needs, i.e. the size of analyzed spicules, and the relation between these spicules (signal) and surrounding background (noise). The size of example spicules in mammograms was experimentally established in previous studies [9]. Thus, two phantoms containing two closely-lying line structures (Fig. 1 - left) were tested. The sample line width of 9 pixels and the line length of 89 or 189 pixels were adopted. To provide adequate (relative to mammographic image) relationship between line structures and background, Gaussian white noise of mean = 0.1 and variance = 3 was added (Fig. 1 – in the middle).

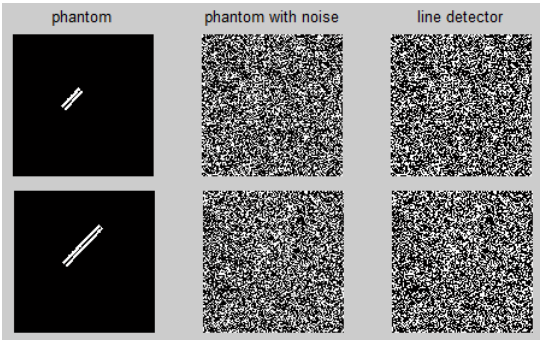

Fig. 1. Two simple phantoms containing: a) two short lines of width 9 pixels and length 89 pixels, b) two longer line structures of width 9 pixels and length 189 pixels. Left to right: phantom of closely-lying lines (rotation angle equals 45 degree), phantom with added noise, and inefficient result of line detector for noisy phantom.

2.1 Angular Resolution versus Structure Rotation

It is commonly known that only some image transformations are shift (rotate) invariant. To verify this aspect, important in line structure recognition process, a simple test was carried out – the line structures on the created phantom were rotated by 20, 50, 90 degrees, respectively. To compare the effectiveness of selected multiscale transformations appropriate MATLAB toolboxes were used. The achieved results presented in Fig. 2 confirm that complex wavelets tend to be the least susceptible to rotation – the image of reconstructed lines are regardless of the rotation angle. In case of complex wavelets there are visible relatively small blur at the ends of the lines on reconstructed images. The accuracy of phantom reconstruction appears to be definitely lower for wavelets, contourlets, and curvelets than complex wavelets. Using wavelets, additional undesirable shadows appear around the reconstructed lines. There is a similar but less visible effect for contourlet transform. However, the curvelets proved to be the least effective tool to enhance the input signal with a small number of coefficients. Curvelets identify and restore lines by isolated "dots", even if a large number coefficients is used. Thus, it is almost impossible to achieve continuous-lines. It is worth noting that the above-mentioned effects will be far more important in interpretation of mammogram contents due to the degree of noise.

2.2 Angular Resolution versus Structure Size

Next, an influence of the number of transformation coefficients on angular resolution was investigated. It has been observed that angular resolution and selectivity is significantly correlated with the number of transformation coefficients. However, it is worth mentioning that the number of coefficients, required to effective line structure reconstruction, depends on several factors. Firstly, it depends on

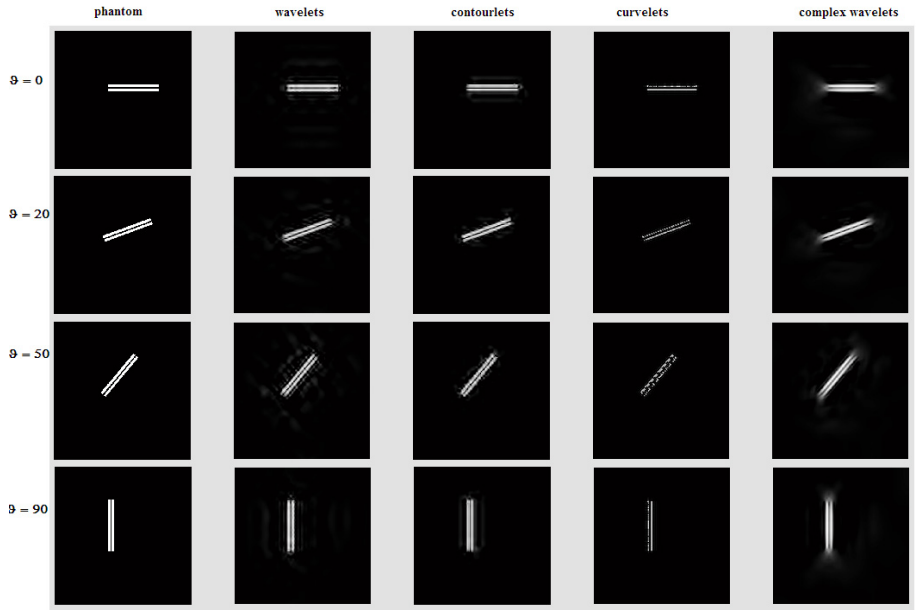

Fig. 2. The phantom of two closely-lying lines of 189 length and four reconstructed images using only 100 significant coefficients of wavelets, contourlets, curvelets, and complex wavelets (left to right). The rotation angle of lines $\theta = 0, 20, 50, 90$ is tested.

the size of analyzed object in image. Secondly, the distance between objects is not meaningless. Therefore, the noisy phantom with lines of $d = 89, 189, 289$ pixels length and the distance between them equal $\Delta = 5$ or 10 pixels, respectively, has been tested. The exemplary results are presented graphically in Fig. 3(a) and Fig. 3(b) – for only $N = 60$ of significant coefficients, and in Fig. 4(a) and Fig. 4(b) – for a much larger number of coefficients, i.e. for $N = 500$.

Comparing the reconstructed image containing lines with different distance (Fig. 3(a) with Fig. 3(b) and Fig. 4(a) with Fig. 4(b)) it appears that line distance is not as significant as length of line. Therefore, further discussion will focus on correlation between the length of different oriented lines and the possibility of their identification.

In order to objectively assess whether two lines are detected in the reconstructed images, the Matlab function *Demirel Edge Detector* was used. Two required parameters were determined experimentally: $T = 0.5$ – a threshold between 0 - 1, and $t = 8$ – the thickness of the line to indicate the edge (the t is 1 pixel smaller than the width of the phantom line due to slightly smaller size of lines in the reconstructed image). The miserable effect of line detector for noisy

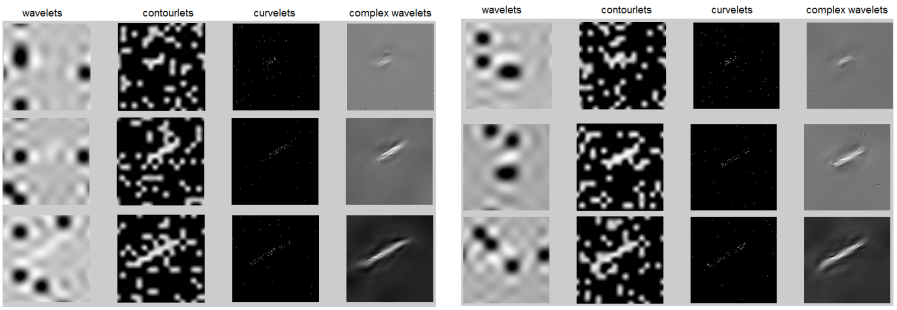

(a) $N = 60, \Delta = 5$ (b) $N = 60, \Delta = 10$

Fig. 3. Visual representation of the impact of line length (from top to bottom: $d = 89, 189, 289$ pixels, respectively) for reconstruction using only $N = 60$ significant coefficients of wavelets, contourlets, curvelets, and complex wavelets (left to right). The rotation angle of line $\theta = 30$, the line distance $\Delta = 5$ or 10 pixels.

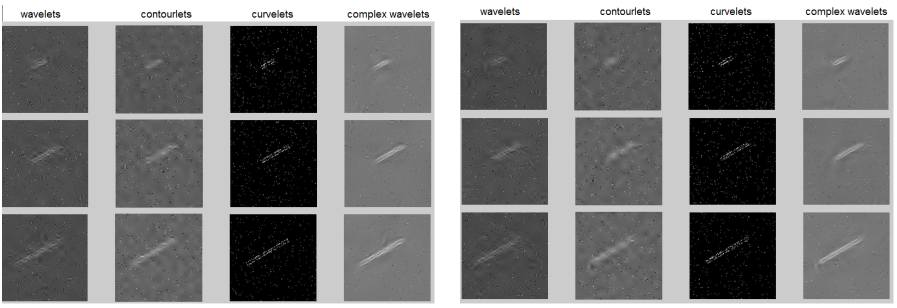

(a) $N = 500, \Delta = 5$ (b) $N = 500, \Delta = 10$

Fig. 4. Visual representation of the impact of line length (from top to bottom: $d = 89, 189, 289$ pixels, respectively) for reconstruction using only $N = 500$ significant coefficients of wavelets, contourlets, curvelets, and complex wavelets (left to right). The rotation angle of line $\theta = 30$, the line distance $\Delta = 5$ or 10 pixels.

phantom of closely-lying lines with distance between them $\Delta = 5$ pixels can be seen in Fig. 1 - right. The noise dominates the signal (line structures). However, the detection of these lines is possible in a situation when the detector is used on the reconstructed images obtained after the removal of a certain number of coefficients. The results for noisy phantom with 189-pixels lines rotated by $\theta = 30$ degree are shown in Fig. 6.

Based on achieved results, it is noteworthy that input signal enhancement, without unnecessary noise, is enabled only using the small number of complex wavelet coefficients (about $N = 60 - 100$). This is also confirmed by the graph in Fig. 5, obtained by use of four multiscale transformations of the noisy phantom

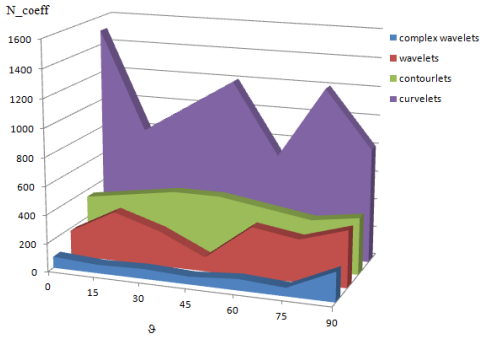

Fig. 5. A sample graph showing a dependence of the number of transformation coefficients N_{coeff} on the rotation angle θ for wavelets, contourlets, curvelets, and complex wavelets, accordingly. This result is achieved for phantom with lines of length $d = 189$ pixels and distance between them $\Delta = 5$.

with 189-pixels lines rotated by angle $\theta = 0 - 90$ degrees. However, it should be mentioned that the number of transformation coefficients required for effective line reconstruction seems to be independent on the length of analyzed structures.

Interpreting the results achieved for wavelets, it is apparent that using the similar to the case of complex wavelets number of coefficients (see in Fig. 6, $N = 400$ and 1000) the reconstruction of two closely-lying lines is also possible, but simultaneously extra noise (constituting useless informations) is extracted. In addition, only for $\theta = 0, 45, 90$ closely-lying lines are quite accurately reconstructed. For other value of θ these line structures connect locally (e.g. for $\theta = 30$ in Fig. 6).

Furthermore, using increasing number of contourlets coefficients to distinguish two closely-lying lines of different rotation angles is impossible. In this situation the energy coefficients focuses not only on the signal but also the noise. Thus, the number of coefficients, useful for the line reconstruction, is limited (see in Fig. 6, $N = 400$ and 1000).

In the case of curvelet transform coefficients failed to keep the continuity of the reconstructed lines (Fig. 3(a), Fig. 4(a), and Fig. 6). Therefore, it is suspected that reconstructed structures tend to be discontinuous even using significantly number of the curvelet transform coefficients.

Summarizing, it is undoubtedly that complex wavelets tend to be very useful tool to investigate image texture directionality due to structure rotate and size invariant. For the same number of the complex wavelet coefficients both the short and long line structures can be enhanced on reconstructed images. Additionally, to reconstruct the input signal without noise the smallest number of the complex wavelet coefficients is sufficient (in comparison to other transformations).

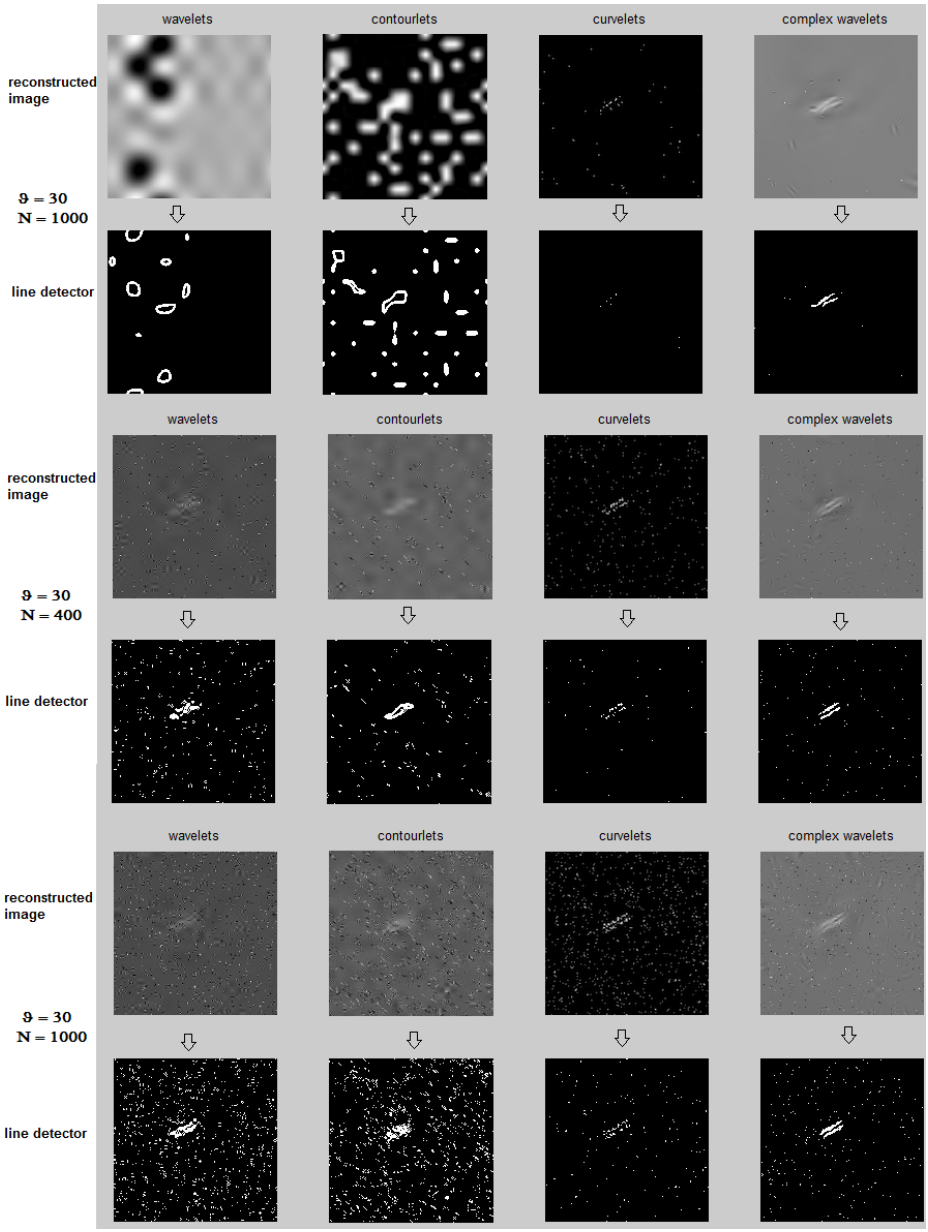

Fig. 6. Noisy phantom of two closely-lying lines ($d = 89$, $\Delta = 5$ pixels) and four reconstructed images using respectively $N = 60, 400, 1000$ significant coefficients of wavelets, contourlets, curvelets, and complex wavelets (from left). Additionally, the effect of line detector was presented. The rotation angle of line $\Theta = 30$ is shown for example.